Supporting Information

Boosting non-sacrificial H_2O_2 production on $Bi_6S_2O_{15}$ photocatalyst via creating a crystal surface-dependent internal electric field

Gaoming Bian[a, b], Chen Wang[c], Yaning Zhang[a, b], Junshan Li[d], Yang Lou[a, b], Ying Zhang[a, b], Yuming Dong[a, b], Jing Xu[e], Yongfa Zhu[a, b, f], and Chengsi Pan[a, b, *]

[a] *Key Laboratory of Synthetic and Biological Colloids, Ministry of Education, School of Chemical and Material Engineering, Jiangnan University, Wuxi, Jiangsu, 214122, China.*

[b] *International Joint Research Center for Photoresponsive Molecules and Materials, Jiangnan University, Wuxi, Jiangsu 214122, China.*

[c] *Harbin Zhongke Materials Engineering Co., Ltd, Harbin, Heilongjiang, 150040, China.*

[d] *Institute for Advanced Study, Chengdu University, Chengdu, 610106, P. R. China.*

[e] *School of Food Science and Technology, Jiangnan University, Wuxi, 214122, PR China.*

[f] *Department of Chemistry, Tsinghua University, Beijing 100084, China.*

[*] *To whom the manuscript should be contact: cspan@jiangnan.edu.cn (C. Pan).*

Experimental Sections

S1. Materials

All chemicals in the experiment were purchased by the National chemical company and used without further purification. The ultrapure water (18.2 MΩ•cm) was used in all the following experiments.

S2. The preparation of HBIP@BSO-110 photocatalyst

HBIP@BSO-110 (Hexagonal $BiPO_4$ coating BSO-110) was synthesized by phosphoric acid etching method. In detail, 0.5 g BSO-110 photocatalyst and 50 μL 1 M H_3PO_4 were put into a beaker containing 30 mL H_2O. After vigorously stirring for 1 h, the uniform suspension was transferred into a 50 mL Teflon-lined stainless-steel autoclave. The hydrothermal reaction was kept at 180 °C for 2 h without shaking and stirring. The rest of the steps were the same as the synthesis of BSO photocatalysts. The HBIP thickness coating BSO-110 was calculated at ca. 3 nm.

S3. Extra characterization of materials

The Zeta potentials of all materials were measured by a Zeta potentiometer (ZetaPALS, Brookhaven, USA). The crystalline phase structure of all materials was characterized via a powder X-ray diffraction (XRD, D8 Bruker, German) with a Cu Ka (1.5418 A) monochromator at 40 kV and 40 mA. The distribution of all elements was characterized by a scanning transmission electron microscope (STEM, FEI Talos F200x G2, USA). The ultraviolet-visible diffuse reflectance spectrum adsorption was studied by ultraviolet-visible spectroscopy with a UV-3600 plus ultraviolet-visible spectrophotometer (UV-Vis DRS, Shimadzu, Japan). The valence state spectrum was recorded with X-ray photoelectron spectroscopy (XPS, Axis Supra instrument, Kratos, UK) with Al Ka monochromatized radiation (hυ=1486.6 eV, 225 W). Raman spectra were recorded on an inVia spectrometer (Renishaw, UK) and a 785 nm YAG laser was used as the excitation source, where the laser power was 5 mW.

S4. Apparent quantum yields (AQY)

AQY measurement was performed in a 20 mL vial. In detail, 5 mg BSO-110 and 10 mL H_2O

were added to the vial and uniformly dispersed by ultrasound. A hole with a diameter of 1 cm was left at the top of the vial for light input, and the rest was covered with Al foil. Then, 99.999% O_2 was continuously bubbled into the solution at a flow rate of 100 ml/min for 30 min to reach oxygen saturation. The 18 W UV lamp was used to irradiate the vial with 4 mW/cm^2 and sampled at certain time intervals. The incident UV light was filtered by a 254 ± 10 nm band-pass filter and monitored with an ultraviolet spectrum analyzer (OHSP-350 UV, Hangzhou, China). The AQY for H_2O_2 formation is calculated by the following equation:

$$AQY(\%)=(H_2O_2 \text{ formed (mol)} \times N_A \times h \times C)/(I \times A \times \lambda \times t) \times 100\%$$

where N_A is the Avogadro constant (6.02×10^{23} mol^{-1}); h is the Planck constant (6.626×10^{-34} J·s); C is the light speed (3.0×10^8 m/s); I is the light intensity (W/m^2/nm); A is the irradiation area (m^2); λ is the wavelength of incident light (nm), and t is the reaction time (s).

Note that in the AQY calculation, the H_2O_2 amount is not multiplied by "2", because our system for H_2O_2 production is from both electron and hole paths. For the system where only O_2 is reduced to H_2O_2 by a single path, the H_2O_2 amount will be multiplied by “2”. This means when the same number of photons are absorbed, the dual paths can produce twice H_2O_2 relative to the single path.

S5. Transient photocurrent and OCP measurement

The transient photocurrent and OCP measurement were performed on a CHI 750 electrochemical workstation. A two-electrode system was used in the experiments, where BSO/FTO glass (1.5 × 1 cm^2) was used as the working electrode, and platinum mesh (1.0 × 1.0 cm^2) was used as the reference electrode and the counter electrode. Other measurement conditions were the same as the three-electrode system listed in the manuscript.

S6. Transient PL measurement

The transient PL spectra of BSO with different exposed surfaces were measured using a

fluorescence lifetime spectrometer (Lifespec II, Edinburgh) equipped with a 375 nm pulse laser (EPL375). Signals were recorded by using the time-correlated single photon counting method.[s1] The transient PL decay curves were fitted on a software (F980) provided by the instrument. The data was fitted by using multiple exponential formula (Eq.s1) , and the average decay time $\bar{\tau}$ was calculated by using the formula (Eq.s2) as reported[s2]:

$$R(t)= B_1 e^{\frac{-t}{\tau_1}} + B_2 e^{\frac{-t}{\tau_2}} + B_3 e^{\frac{-t}{\tau_3}} \cdots\cdots\cdots\cdots \text{Eq.s1}$$

$$\bar{\tau} = \frac{B_1\% \times \tau_1^2 + B_2\% \times \tau_2^2 + B_3\% \times \tau_3^2}{B_1\% \times \tau_1 + B_2\% \times \tau_2 + B_3\% \times \tau_3} \cdots\cdots \text{Eq.s2}$$

Where B_1, B_2, and B_3 represent the amplitudes of the fast and slow components, and τ_1, τ_2, and τ_3 represent the time constants.

S7. DFT

The electronic structure properties of BSO were calculated by a CASTEP package in Material Studio[s3]. DFT calculations were performed using a 1×1×1 primitive cell of BSO. The exchange-correlation energy is calculated by the Generalized Gradient Approximation (GGA) with the Perdew-Burke-Ernzerhof (PBE) functional. The wave function is expanded using a plane-wave basis with a cut-off energy of 380 eV and a Monkhorst-Pack grid with a 3×3×3 K-point mesh for the integration in the Brillouin zone. The geometric optimization conditions are as follows: The electronic minimization parameter of the total energy/atom convergence tolerance energy per atom < 2×10^{-5} eV; the stress tolerance stress < 0.1 GPa; the force < 0.05 eV/Å; and the ionic displacement < 2×10^{-3}Å.

Results and Discussion

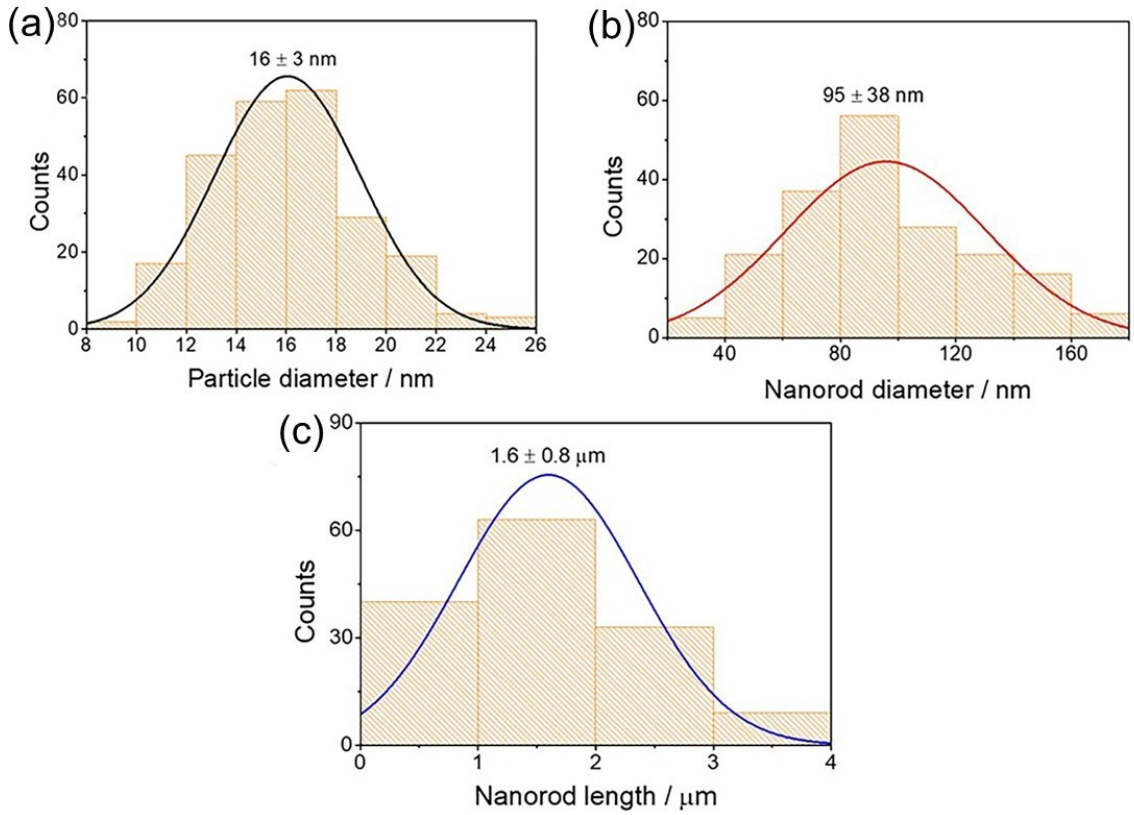

Fig. S1 (a) The particle diameter distribution diagram of BSO particles, (b) the nanorod diameter, and (c) length distribution diagram of BSO nanorods.

Table S1. Zeta potential of BSO photocatalysts with different exposed surfaces

Samples	Zeta-1 / mV	Zeta-2 / mV	Zeta-3 / mV	Zeta-4 / mV	Zeta-5 / mV	Zeta-Average / mV
BSO-$\bar{1}$30	-41.08	-36.91	-39.09	-37.97	-40.06	-39.02 ± 1.65
BSO-110	-30.93	-34.73	-35.89	-31.00	-32.48	-33.01 ± 2.23
BSO-400	-24.05	-27.57	-25.56	-27.08	-25.82	-26.01 ± 1.38

The Zeta potentials of BSO photocatalysts with different exposed surfaces were measured by a potentiometer (ZetaPALS, Brookhaven). The average Zeta potential changes in flowing order: BSO-$\bar{1}$30 (-39.02 mV) > BSO-110 (-33.01 mV) > BSO-400 (-26.01 mV). The result indicates that BSO-$\bar{1}$30 has the most negative Zeta potential relative to BSO-110 and BSO-400, which may be due to the large electrostatic repulsion between individual particles, as reported[s4].

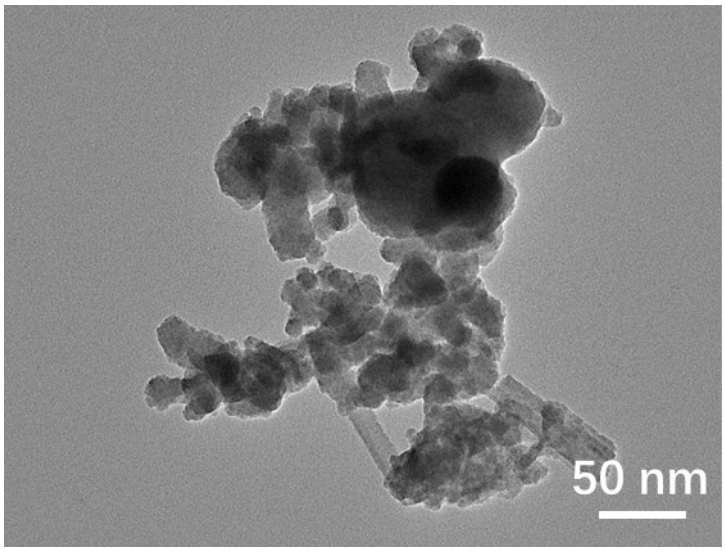

Fig. S2 TEM of BSO photocatalyst hydrothermally prepared at 150 ^{o}C.

Fig. S2 shows the BSO TEM image prepared at 150 ^{o}C, and the phenomenon that agglomerated particles tend to fuse together is observed. The diameter of the nanorods is 6 times as large as that of nanoparticles as shown in Fig. S1, suggesting the nanorod may form from the agglomeration of the particle.

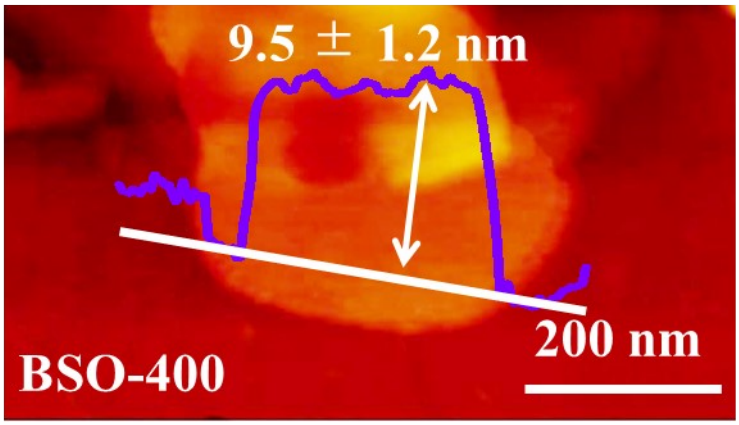

Fig. S3 AFM image of BSO nanoplates.

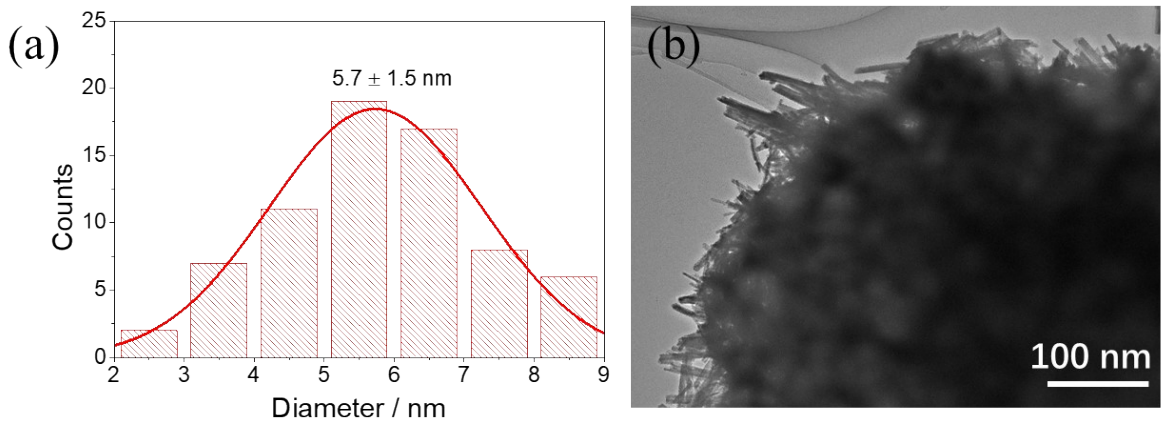

Fig. S4 (a) The nanorod diameter distribution diagram, and (b) TEM of BSO photocatalyst hydrothermally prepared at 220 °C.

Fig. S4 shows the nanorod diameter diagram and TEM image of BSO prepared at 220 °C. The tiny nanorod-like grains (diameter 5.7 ± 1.5 nm) cross stacking is observed, while the nanosheet (obtained at 240 °C) show a layered structure with a thickness of 9.5 ± 1.2 nm as shown in Fig. S3, indicating the nanosheets may be formed due to cross stacking of the tiny nanorod-like grains.

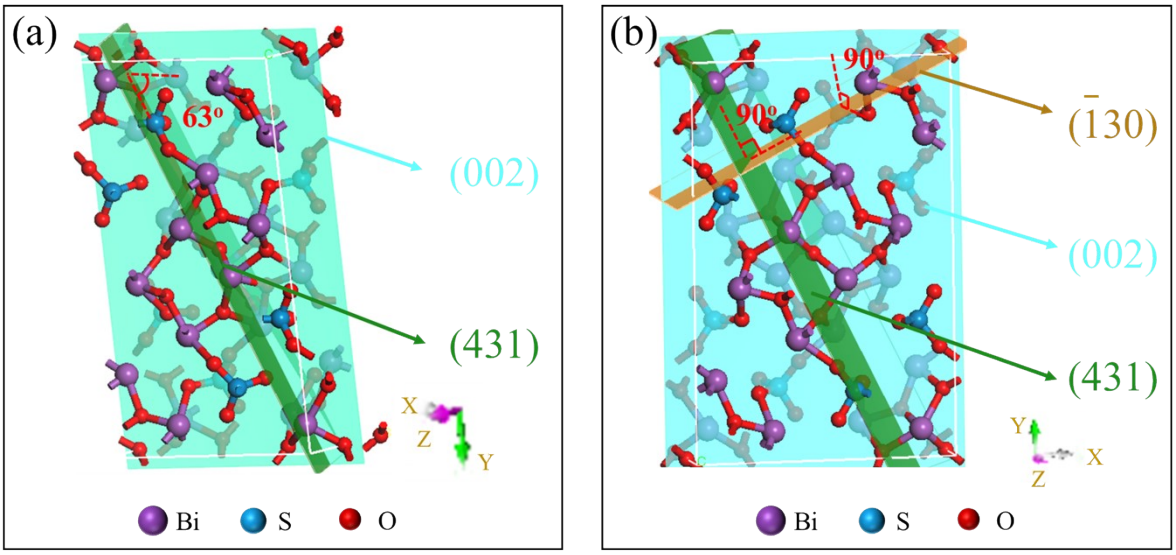

Fig. S5 (a) Geometrical relationship between (002) planes and (431) planes, (b) Vertical relationship between (002) planes and (−130) planes, between (431) planes and (−130) planes.

The schematic diagram of the BSO crystal structure (Fig. S5) shows the detailed geometric relationship: the (002) plane is at a 63° angle to the (431) plane, which correspond to the result of HRTEM in Fig. 1c; the (002) plane and the (−130) plane are vertical with each other; the (431) plane and the (−130) plane are vertical with each other, indicating the plane exposed on BSO particle is the (−130) plane.

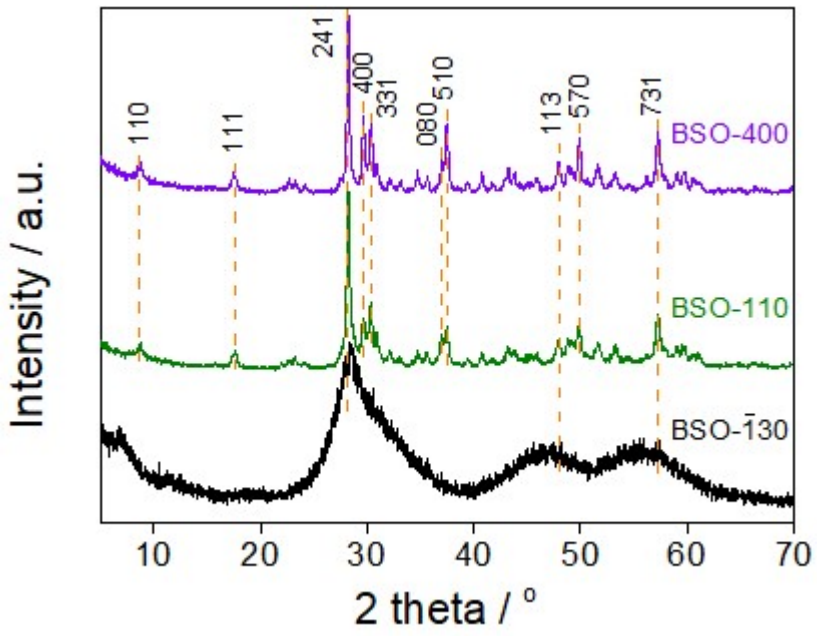

Fig. S6 XRD patterns of BSO photocatalysts prepared at different hydrothermal temperatures with different exposed faces.

For BSO-$\bar{1}$30, XRD peaks locating at 28.2°, 47.4 °, 55.6 °, and 57.2 ° are observed, while for BSO-110 and BSO-400, extra peaks located at 8.7°, 17.5°, 29.7°, 30.4°, 37.0, 37.5°, and 49.9° emerge. No additional diffraction peaks or impurities were observed in the XRD pattern, indicating that the prepared BSO samples were pure phase. All three samples showed XRD peaks corresponding to standard BSO patterns reported in the literature[s5].

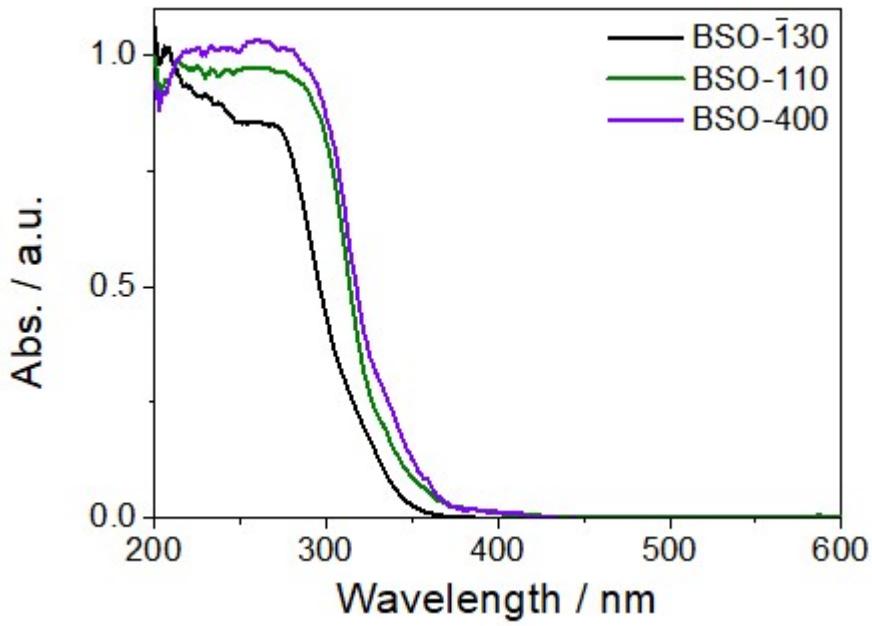

Fig. S7 UV-Vis DRS spectra of BSO photocatalysts with different exposed faces.

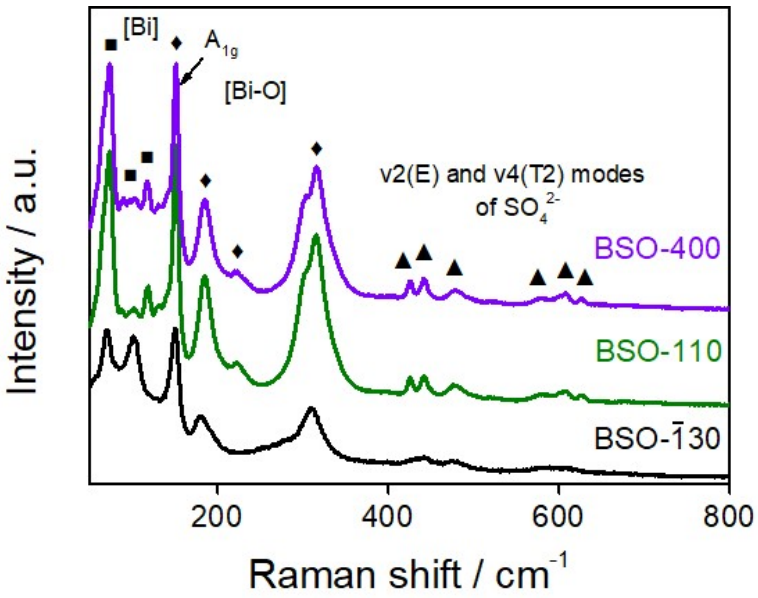

Fig. S8 Raman spectra of BSO photocatalysts with different exposed faces.

Raman spectra in Fig. S8 show the lattice vibration of the three samples. The vibration modes observed at below 150 cm^{-1} can be assigned to Bi atoms, between 150-400 cm^{-1} can be assigned to Bi-O vibration, and above 400 cm^{-1} can be assigned to vibrational modes of SO_4^{2-}. For BSO-110 and BSO-400, triplet peaks located at 425, 441, and 478 cm^{-1}, and 578, 609, and 628 cm^{-1} are observed, which corresponds to the v2(E) bending mode and v4(T2) vibrational modes of SO_4^{2-}, respectively.[s5-7] The extra Raman peaks emerge for the well-crystallized samples as reported in literature. The relative intensities of Bi-O in [BiO6] octahedron located at 151, 185, 222, and 315 cm^{-1} change obviously with increasing hydrothermal temperature.

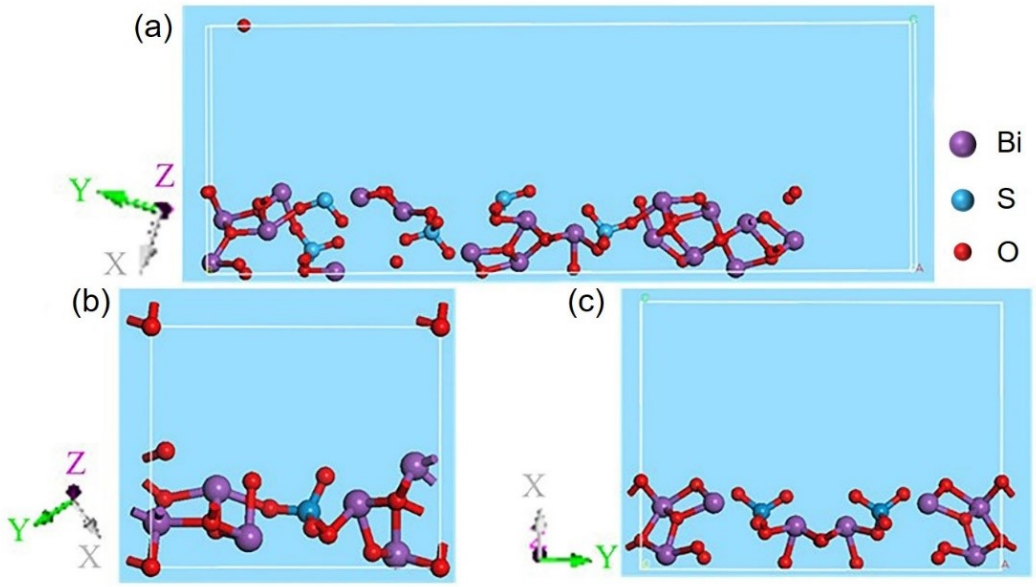

Fig. S9 The crystal structure of exposing (a) (−130) surfaces, (b) (110) surfaces, and (c) (400) surfaces.

The crystal structures of different exposed surfaces are obtained a thickness of 5 Å. The ratio of the number of Bi atoms and S atoms changes in the following order: (110) > (400) > (−130). This indicates that there are more distorted [BiO3] and [BiO6] polyhedrons on the (110) surfaces exposed on BSO-110 relative to the (400) surfaces exposed on BSO-400 and the (−130) surfaces exposed on BSO-$\bar{1}$30. More Bi-O bonding on (110) surfaces may lead to more distorted [BiO3] and [BiO6] polyhedron by increasing the lattice dipole of the sample, which will benefit for the charge separation and transfer and enhancing the photocatalytic activity.

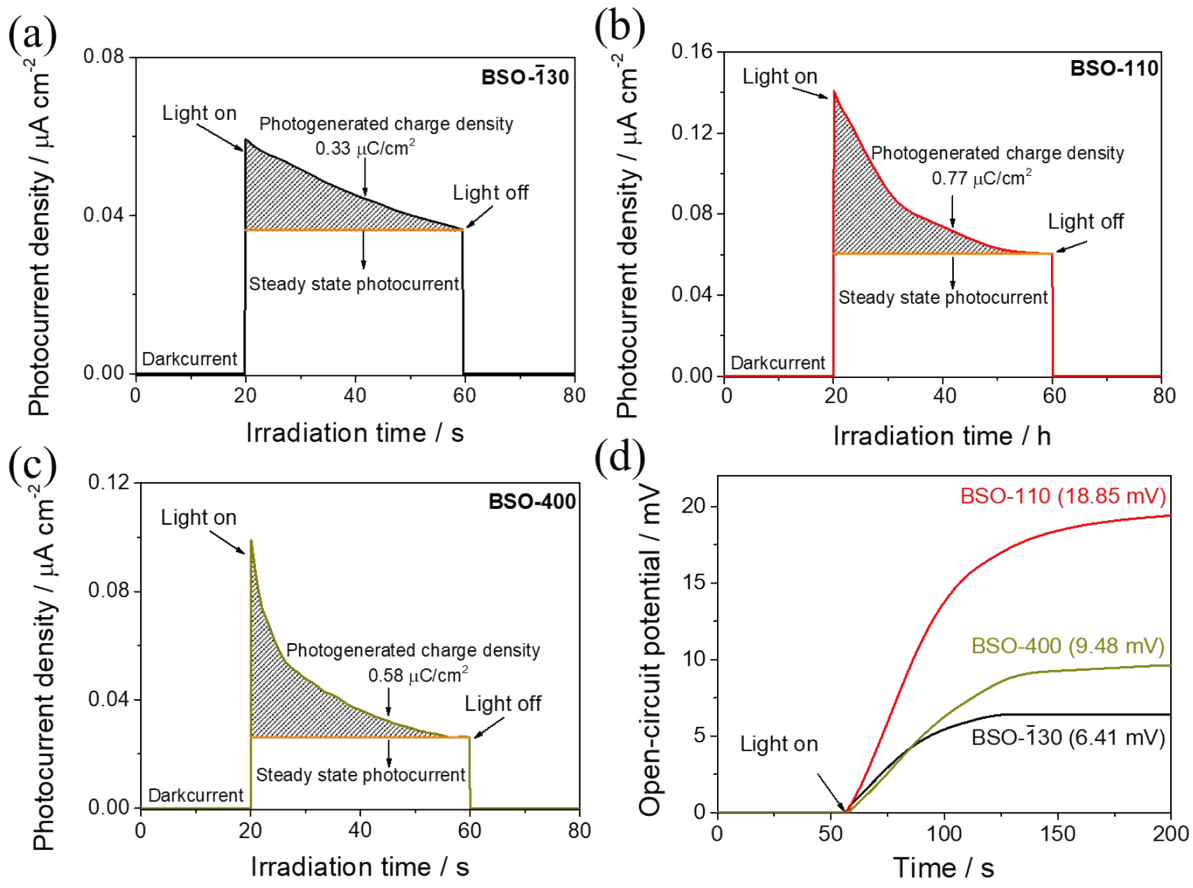

Fig. S10 Transient photocurrent of (a) BSO-$\bar{1}$30, (b) BSO-110, and (c) BSO-400; (d) OCP measurement of three exposed planes on BSO photocatalysts.

The photo-generated charge density and open circuit potential of BSO photocatalysts with three exposed planes were measured to evaluate the IEF as shown in Fig. S10. Fig. S10a-c show the photo-generated charge density of BSO-$\bar{1}$30, BSO-110, and BSO-400, respectively, which changes as follows: BSO-110 (0.77 μC/cm^2) > BSO-400 (0.58 μC/cm^2) > BSO-$\bar{1}$30 (0.33 μC/cm^2). By integrating the measured transient photocurrent density minus the steady-state photocurrent value with respect to time, the IEF is proportional to the number of charges accumulated on the surface as reported[s2, 8]. Fig. S10d show the results of the open circuit potential, which changes as follows: BSO-110 (18.85 mV) > BSO-400 (9.48 mV) > BSO-$\bar{1}$30 (6.41 mV).

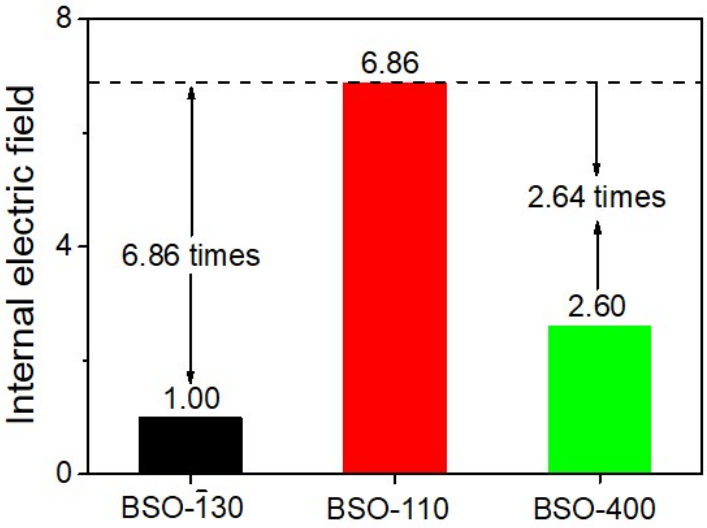

Fig. S11 The intensity of internal electric field on BSO-$\bar{1}$30, BSO-110, and BSO-400 photocatalysts (assuming the intensity of the internal electric field in BSO-$\bar{1}$30 is "1").

The IEF of BSO-$\bar{1}$30, BSO-110, and BSO-400 were calculated by using the following equation s3[s2, 8], and the intensity of the IEF in BSO-$\bar{1}$30 was assumed to be "1". It can be found that the IEF intensity of BSO-110 is 6.86, 2.64 times as high as that of BSO-$\bar{1}$30 and BSO-400, respectively (Fig. S10).

$$E = \left(\frac{-2V_s\rho}{\varepsilon\varepsilon_0}\right)^{1/2} \cdots\cdots\cdots\cdots\cdots \quad \text{Eq. s3}$$

Where E is the IEF magnitude, V_s is the surface voltage, ρ is the surface charge density, Ɛ is the low-frequency dielectric constant, and $Ɛ_0$ is the permittivity of free space. The above equation reveals that the IEF magnitude is mainly determined by the surface voltage and the charge density because Ɛ and $Ɛ_0$ are two constants.

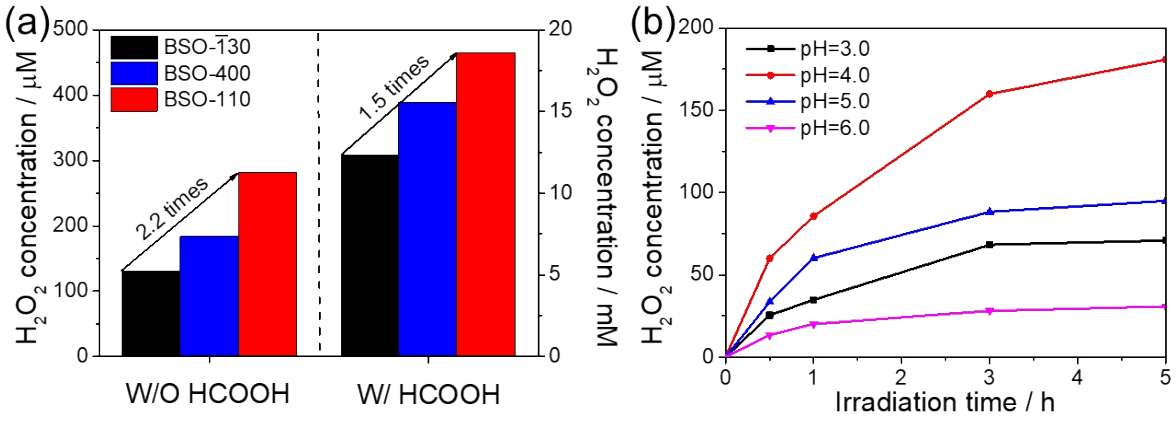

Fig. S12 (a) H_2O_2 production after 5 h irradiation with and without sacrificial regents. Reaction conditions: 25 mg cat., 50 mL H_2O (pH = 4.0) or 50 mL 10 vol % HCOOH aq, 18 W UV-254 nm lamp. (b) The activity of H_2O_2 production on BSO under different pHs. Reaction conditions: 25 mg cat., 50 mL H_2O, 18 W UV-254 nm lamp. The pH is adjusted by 1 M HCl.

Fig. S12a shows the H_2O_2 production after 5 h irradiation with and without sacrificial regents under UV-254 nm lamp. Although the addition of HCOOH increased the H_2O_2 concentration, the activity difference between the three BSO photocatalysts with the highest activity and lowest did not change relative to Xe lamp irradiation, indicating the activity difference between three samples is mainly influenced by the IEF rather than the exciting energy.

The pH influence on the BSO-110 activity is shown below and in Fig. S12b. From the results, the activity increases with the pH changing from 6.0 to 4.0, and decreases with further increasing the pH. The increase may be because the acidic condition will increase the stability of the produced H_2O_2. The decrease may be due to the breakdown of BSO structure in an over acidic condition.

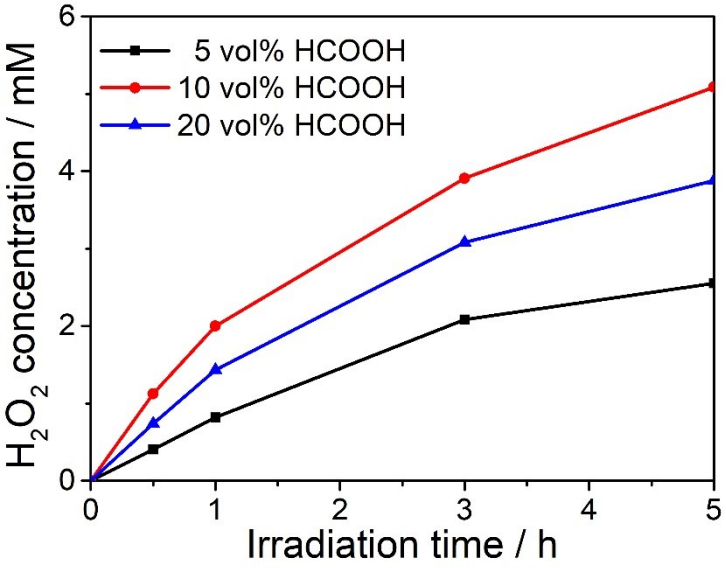

Fig. S13 The H_2O_2 production activity on BSO with different HCOOH concentrations. Reaction conditions: 25 mg cat., 50 mL solvent, 300 W Xe lamp ($\lambda > 300$ nm).

To understand the influence of HCOOH concentration on H_2O_2 production activity, we have added 5 vol% HCOOH and 20 vol% HCOOH to the reaction solution, as shown in Fig. S13. From the results, the activity increases with the HCOOH concentration changing from 5 vol% to 10 vol%, and decreases with further increasing the concentration. The H_2O_2 production activity increase with HCOOH concentration is because the increase of HCOOH content effectively increases the charge separation efficiency in BSO photocatalysts. But with further addition of HCOOH (20 vol%), the BSO partially dissolved because HCOOH is a strong coordination reagent. Thus, the activity decreased rapidly.

Table S2. Activity comparison of BSO-110 photocatalysts with other reported systems for H_2O_2 production from only H_2O and O_2.

Photocatalysts	**Sln.**	**Solvent (ml)**	**Cat. (mg)**	**Light source**	**H_2O_2 production rate / μM/h**	**H_2O_2 accumulation for 5 h / μM**	**Ref.**
BSO-110	H_2O (pH=4.0)	50	25	300 W Xe lamp (λ>300 nm)	80	180	This work
BSO-110	H_2O (pH=4.0)	50	25	18 W UV-254 nm lamp	140	280	This work
$BiPO_4$	H_2O	50	25	300 W Xe lamp (λ>300 nm)	0	0	s9
$BiPO_4$	H_2O	50	25	18 W UV-254 nm lamp	300	1000	s9
$BiVO_4$	H_2O	30	50	2 kW Xe lamp (λ>420 nm)	1	5	s10
Bi_2WO_6	H_2O	50	65	150 W Xe lamp (λ>400 nm)	25	25 (1 h)	s11
TiO_2	H_2O	30	30	500 W simulated sunlight (λ > 300 nm).	10	20	s12
ZnO	H_2O	50	-	9 W UV-365 nm lamp	0.4	1.4	s13
CdS/S-carbon[+]	H_2O	25	25	300 W Xe lamp	566	1700 (3 h)	s14
MoS_2	H_2O	50	50	300 W Xe lamp (λ>420 nm)	50	150	s15
$Cu_2(OH)PO_4$[+]	H_2O	200	200	300 W Xe lamp	40	200 (5 h) 230 (18 h)	s16
MoO_3/SnS_2	H_2O	100	50	Solar simulator	70	140 (3 h)	s17

N doped Cu_2O^+/CuO	H_2O	10	15	300 W Xe lamp	12	12 (1 h)	s18

[+] Activity decay dramatically after 3-5 h irradiation due to the introduction of unstable species like Cu^I or S^{2-}.

Table S3. Activity comparison of BSO-110 photocatalysts with other reported systems for H_2O_2 production in the presence of organic sacrificial.

Photocatalysts	Sln.	Solvent (ml)	Cat. (mg)	Light source	H_2O_2 production rate / mM/h	H_2O_2 accumulation for 5 h / mM	Ref.
BSO-110	10 vol % HCOOH	50	25	300 W Xe lamp (λ>300 nm)	2.0	5.1	This work
BSO-110	10 vol % HCOOH	50	25	18 W UV 254 nm lamp	11.2	19.6	This work
$Pd/BiVO_4$	10 vol % MeOH (PBS)	50	-	300 W Xe lamp (λ>420 nm)	0.3	0.6 (2 h)	s19
BiOCl[*]	4 vol % HCOOH	100	50	500 W Xe lamp	10.2	12.2 (2 h) 11.6 (3 h)	s20
BiOBr	10 vol % IPA (2 M HCl)	50	50	5 W LED lamp	0.34	0.57 (2 h)	s21
TiO_2	130 mM Furfural alcohol	30	30	500 W Xe lamp (λ > 300 nm)	0.6	1.0 (2 h)	s12
ZnO	4 vol % EtOH	200	200	300 W Xe lamp	0.05	0.2	s22
Ag_3PO_4	10 vol % MeOH	100	100	AM1.5	0.09	0.14	s23
Au/WO_3	4 vol % MeOH	50	50	400 W Halide lamp (λ > 420 nm)	0.18	0.55	s24
$TiO_2/Co_3O_4/Ni$	20 vol % MeOH	50	50	300 W Xe lamp	0.11	0.33	s25
$Au/SnO_2/TiO_2$	4 vol % EtOH (0.1 M NaF)	200	200	300 W Xe lamp	0.8	3.8	s26
KPF_6/BiOBr	10 vol % IPA	50	50	5 W LED lamp	1.1	1.25 (2 h)	s21

	(2 M HCl)						
$Au/TiO_2/Bi_2O_3$	4 vol % EtOH	200	200	300 W Xe lamp	1.0	4.8	s27

* Activity decay dramatically after 2 h irradiation due to the instable chemical compositions.

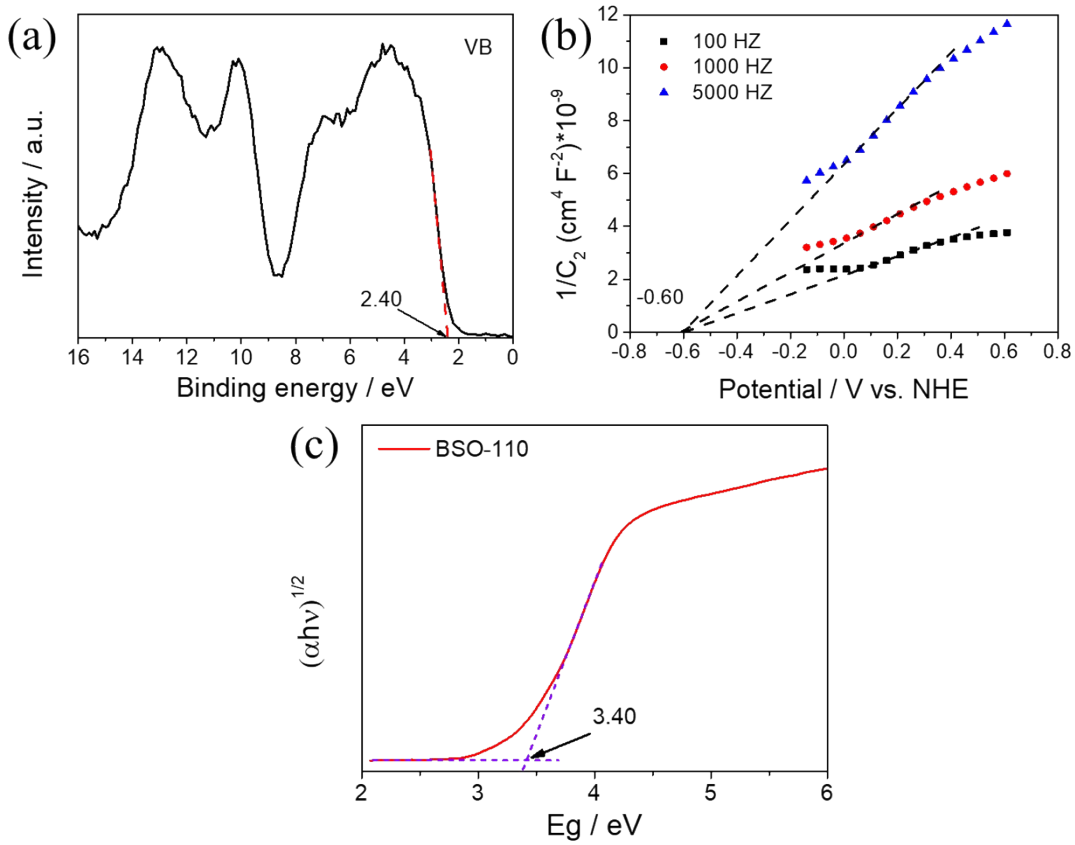

Fig. S14 (a) XPS valence spectrum, (b) Mott-Schottky plots measured on 100 HZ, 1000 HZ, and 5000 HZ, and (c) Tauc plot of the prepared BSO-110 photocatalyst.

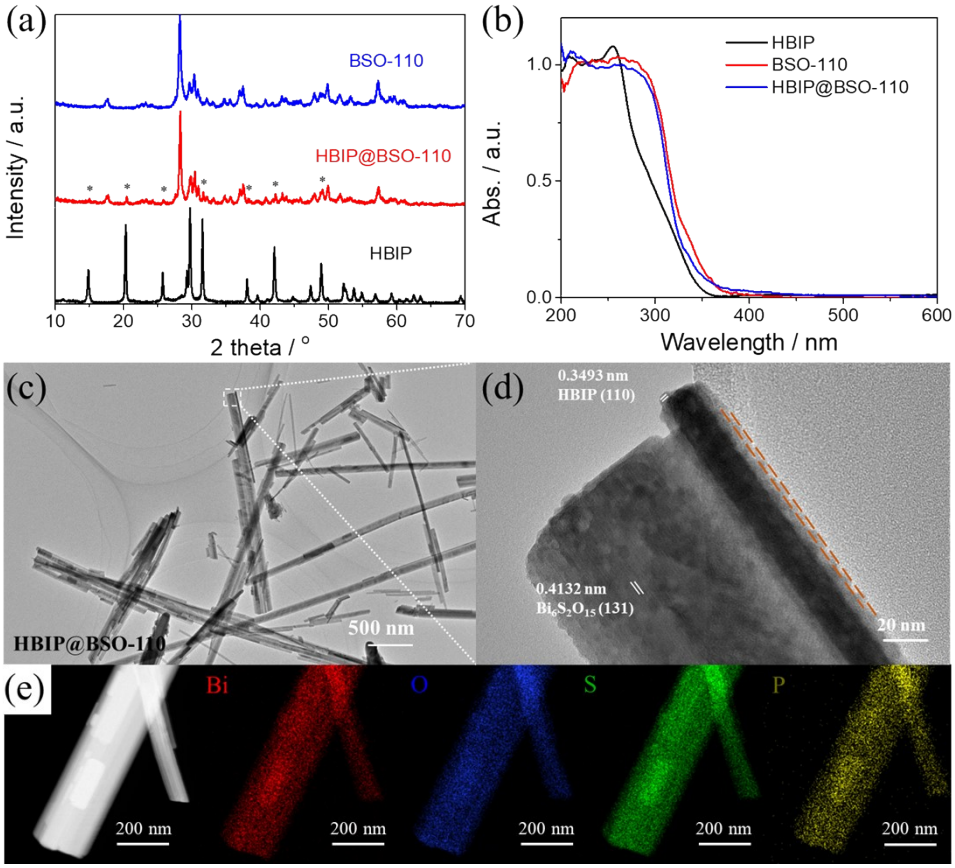

Fig. S15 (a) XRD and (b) UV-Vis DRS patterns of HBIP, BSO-110, and HBIP@BSO-110. (c) TEM, (d) HRTEM, and (e) STEM elemental mapping of BSO-110.

Fig. S15a shows the XRD results of HBIP, BSO-110, and HBIP@BSO-110 photocatalysts. After coating HBIP, the HBIP@BSO-110 photocatalyst appears with new diffraction peaks at 14.9°, 20.5°, 25.8°, 31.7°, 38.3°, 42.2°, and 49.1°, which belong to the characteristic peaks of HBIP photocatalyst. Fig. S15b shows the UV-Vis DRS results of HBIP, BSO-180, and HBIP@BSO-110 photocatalysts. After coating HBIP, the DRS profile of HBIP@BSO-110 exhibits a similar result to our previous work[s9], that is, one part is similar to HBIP and the other part is similar to BSO-110. Fig. S15c show the TEM result of HBIP@BSO-110, and Fig. S15d is the corresponding HRTEM. The lattice fringes of 0.3493 nm in the shell and 0.4132 nm in the core correspond to the (110) faces of HBIP and the (131)

faces of BSO-110 photocatalysts, respectively. Fig. S15e shows the element mapping results of HBIP@BSO-110, where the P element in HBIP is uniformly distributed on the surface of BSO-110. HBIP photocatalyst is successfully coated on the surface of the BSO-110 photocatalyst (HBIP@BSO-110) by the phosphoric acid etching method.

Table S4. The fitting data of transient PL on BSO photocatalysts with different exposed surfaces.

Samples	τ_1 / ns	τ_2 / ns	τ_3 / ns	B_1%	B_2%	B_3%	$\bar{\tau}$ / ns
BSO-$\bar{1}$30	0.94655	4.26756	0.31725	0.65180	0.20930	0.13890	1.55
BSO-110	1.52808	7.97718	0.39918	0.46450	0.38090	0.15460	3.81
BSO-400	0.90049	4.64624	0.17453	0.39890	0.51930	0.08180	2.79

The transient PL fitting data are shown in Table S4, in which the BSO-110 photocatalyst shows the longest decay time among the three catalysts, revealing that the (110) planes exposed on BSO-110 are more efficient for charge separation and transfer relative to (400) planes exposed on BSO-400 and (−130) planes exposed on BSO-$\bar{1}$30.

Table S5. The fitting data of EIS spectra on BSO photocatalysts with different exposed surfaces.

Sample	Rs (Ω)	R_{ct} (KΩ)	CPE (μF)	n
BSO-$\bar{1}$30	111.51	25.50	115.13	0.822
BSO-110	180.22	15.45	122.91	0.790
BSO-400	165.98	20.01	183.60	0.793

The fitting data used for the curves are listed in Table S5, in which Rs, Rct, and CPE represent the solution resistance, the charge transfer resistance, and the constant phase element for the electrolyte/electrode interface, respectively. The Rct of BSO-110 is the smallest relative to BSO-$\bar{1}$30 and BSO-400, which proves that BSO-110 with the strongest IEF is most suitable for charge transfer.

References

s1 L. Dai, J. Liu, K. Liang, R. Yang, D. Han and B. Lu, *Biomed. Opt. Express*, 2020, **11**, 2205-2212.

s2 Y. Zhang, D. Wang, W. Liu, Y. Lou, Y. Zhang, Y. Dong, J. Xu, C. Pan and Y. Zhu, *Appl. Catal. B Environ.*, 2022,**300**, 120762.

s3 S. J. Clark, M. D. Segall, C. J. Pickard, P. J. Hasnip, M. I. J. Probert, K. Refson and M. C. *Payne*, 2005, **220**, 567-570.

s4 E. Joseph and G. Singhvi, *Nanomaterials for Drug Delivery and Therapy, William Andrew Publishing*, 2019, pp.91-116.

s5 J. Wang, W. Jiang, D. Liu, Z. Wei and Y. Zhu, *Appl. Catal. B Environ.*, 2015, **176-177**, 306-314.

s6 L. Kumari, J. H. Lin and Y. R. Ma, *J. Phys. Condens. Matter.*, 2007, **19**, 406204.

s7 J. Geng, W.-H. Hou, Y.-N. Lv, J.-J. Zhu and H.-Y. Chen, *Inorg. Chem.*, 2005, **44**, 8503-8509.

s8 Y. Guo, W. Shi and Y. Zhu, *EcoMat*, 2019, **1**, e12007.

s9 C. Pan, G. Bian, Y. Zhang, Y. Lou, Y. Zhang, Y. Dong, J. Xu and Y. Zhu, *Appl. Catal. B Environ.*, 2022, **316**, 121675.

s10 H. Hirakawa, S. Shiota, Y. Shiraishi, H. Sakamoto, S. Ichikawa and T. Hirai, *ACS Catalysis*, 2016, **6**, 4976-4982.

s11 J. Sheng, X. Li and Y. Xu, *ACS Catal.*, 2014, **4**, 732-737.

s12 J. Zhang, L. Zheng, F. Wang, C. Chen, H. Wu, S. A. K. Leghari and M. Long, *Appl. Catal. B Environ.*, 2020, **269**, 118770.

s13 Y. Liu, J. Han, W. Qiu and W. Gao, *Appl. Surf. Sci.*, 2012, **263**, 389-396.

s14 J. H. Lee, H. Cho, S. O. Park, J. M. Hwang, Y. Hong, P. Sharma, W. C. Jeon, Y. Cho, C. Yang, S. K. Kwak, H. R. Moon and J.-W. Jang, *Appl. Catal. B Environ.*, 2021, **284**, 119690.

s15 H. Song, L. Wei, C. Chen, C. Wen and F. Han, *J. Catal.*, 2019, **376**, 198-208.

s16 X. Wang, Z. Han, L. Yu, C. Liu, Y. Liu and G. Wu, *ACS Sustain. Chem. Eng.*, 2018, **6**, 14542-14553.

s17 Y. Zhang and S.-J. Park, *J. Mater. Chem. A*, 2018, **6**, 20304-20312.

s18 W. Zhang, X. Chen, X. Zhao, M. Yin, L. Feng and H. Wang, *Appl. Surf. Sci.*, 2020, **527**, 146908.

s19 K. Fuku, R. Takioka, K. Iwamura, M. Todoroki, K. Sayama and N. Ikenaga, *Appl. Catal. B Environ.*, 2020, **272**.

s20 Y. Su, L. Zhang, W. Wang and D. Shao, *ACS Sustain. Chem. Eng.*, 2018, **6**, 8704-8710.

s21 C. Du, W. Feng, S. Nie, J. Zhang, Y. Liang, X. Han, Y. Wu, J. Feng, S. Dong, H. Liu and J. Sun, *Sep. Purif. Technol.*, 2021, **279**, 119734.

s22 X. Meng, P. Zong, L. Wang, F. Yang, W. Hou, S. Zhang, B. Li, Z. Guo, S. Liu, G. Zuo, Y. Du, T. Wang and V. A. L. Roy, *Catal. Commun.*, 2020, **134**, 105860.

s23 X. Ma and H. Cheng, *Chem. Eng. J.*, 2022, **429**, 132373.

s24 Y. Wang, Y. Wang, J. Zhao, M. Chen, X. Huang and Y. Xu, *Appl. Catal. B Environ.*, 2021, **284**, 119691.

s25 T. Li, J.-D. Cui, M.-L. Xu, R. Li, L.-M. Gao, P.-L. Zhu, H.-Q. Xie and K. Li, *CrystEngComm*, 2020, **22**, 5620-5627.
s26 G. Zuo, B. Li, Z. Guo, L. Wang, F. Yang, W. Hou, S. Zhang, P. Zong, S. Liu, X. Meng, Y. Du, T. Wang and V. A. L. Roy, *Catal.*, 2019, **9**, 623.
s27 L. Feng, B. Li, Y. Xiao, L. Li, Y. Zhang, Q. Zhao, G. Zuo, X. Meng and V. A. L. Roy, *Catal. Commun.*, 2021, **155**, 106315.